The Clear-Sky Unpolarized Forward Model for the EOS Aura Microwave Limb Sounder (MLS)

William G. Read, Zvi Shippony, Michael J. Schwartz, Nathaniel J. Livesey, and W. Van Snyder

Abstract—**This paper describes the Earth Observing System (EOS) Aura Microwave Limb Sounder (MLS) forward model for a clear-sky atmosphere emitting unpolarized radiation. This model is used for the majority of the EOS MLS radiance calculations. The orbital and viewing geometry of MLS on Aura is such that a two-dimensional (vertical and line-of-sight, horizontal) forward model provides the most accurate basis for the inversion performed in retrievals. The model consists of atmospheric radiative transfer convolved with the instrumental field of view and the spectral response. An additional model relating the pointing heights supplied by the Aura satellite operations and MLS scan pointing encoders to the limb tangent pressure and atmospheric temperature is described. The analytic computation of Jacobians needed for retrievals is given.**

Index Terms—**Aura, Earth Observing System (EOS), Microwave Limb Sounder (MLS), radiative transfer, spectroscopy.**

I. INTRODUCTION

THE Microwave Limb Sounder (MLS) [1], [2] is one of four instruments on the Earth Observing System (EOS) Aura satellite that was launched into a nearly polar low Earth orbit on July 15, 2004. The Aura mission objective is to study the Earth's ozone, air quality, and climate [2]. EOS MLS contributes to this objective by measuring temperature, several key molecules: O_3, H_2O, BrO, CH_3CN, ClO, CO, HCl, HCN, HNO_3, HO_2, HOCl, N_2O, OH, SO_2, and ice water content (IWC) of clouds.

EOS MLS measures atmospheric thermal emission signals at targeted frequencies spanning 118–2500 GHz (2500–120-μm wavelengths). The instrument contains double sideband heterodyne radiometers, except for the 118-GHz radiometer which only receives the lower frequency sideband. The details of the radiometric measurement are given [3]. The spectral coverage of all the MLS bands is shown in Fig. 1. The radiometers and bands are deployed to optimize measurements of the targeted constituents [2].

Aura is in a sun-synchronous polar orbit (98.14° inclination at 705 km). The forward viewing geometry of EOS MLS gives measurements from 82°S to 82°N. Vertical profiles of spectra are measured through separate GHz and THz optics which perform independent limb scans. A complete vertical scan takes 24.7 s, and there are 240 scans per orbit giving

$\sim$3500 scans per day. The limb tangents of the GHz and THz scans proceed from near the surface to 95 km in a continuous movement with measurements taken every 1/6 s. The upward scan movement largely compensates for the satellite forward motion and results in a nearly vertical locus of the tangent point during the scan as shown in [4, Fig. 1]. EOS MLS makes a limb scan every 1.5° of great circle arc. A radiance limb ray whose tangent height is 20 km is below 80 km (i.e., within the region of the atmosphere targeted by MLS) for 16° great circle arc. Accordingly, the horizontal (great circle arc) extent of an individual limb ray is observed by several consecutive radiance scans. Taking advantage of the forward looking geometry and simultaneously retrieving many atmospheric profiles from a consecutive series of radiance scans, the full impact of vertical and horizontal gradients is accurately accounted for [5].

This paper describes the EOS MLS forward model that is used to retrieve constituents [4] from the measured emission. Extensions of the model to include cloud effects and polarized mesospheric O_2 emission are in [6] and [7], respectively. The EOS MLS forward model is the two-dimensional (2-D) extension of the forward model used for the Upper Atmosphere Research Satellite (UARS) [1], [8]–[11]. Similar 2-D radiative transfer models exist that are described in [12]–[16]. The EOS MLS forward model in addition to computing radiances for an atmosphere with horizontal gradients also includes analytical computation of 2-D Jacobians for temperature, concentrations and spectral parameters such as line width; however, it is noted that analytical calculation of Jacobians is a feature of other forward models [12]–[14]. The EOS MLS forward model is designed for direct interface to the EOS MLS geophysical parameter retrievals (Level 2) [4]. The forward model has an additional scan residual model that computes the GHz and THz limb tangent heights from their limb tangent pressures.

Fig. 2 shows a schematic of the EOS MLS forward model where each oval shows the section in the paper describing each operation and the rectangular boxes show the data required for or produced from that operation. The radiance forward model performs the following calculations.

1) *Ray tracing* evaluates the atmospheric state [height, pressure, temperature, molecular compositions, and volume mixing ratio (VMR)] along the limb line-of-sight (LOS).
2) *Cross-section calculation* computes the absorption cross sections along the LOS for the predefined frequency grid.
3) *Radiative transfer* calculates the monochromatic, single-ray radiances for these frequencies.
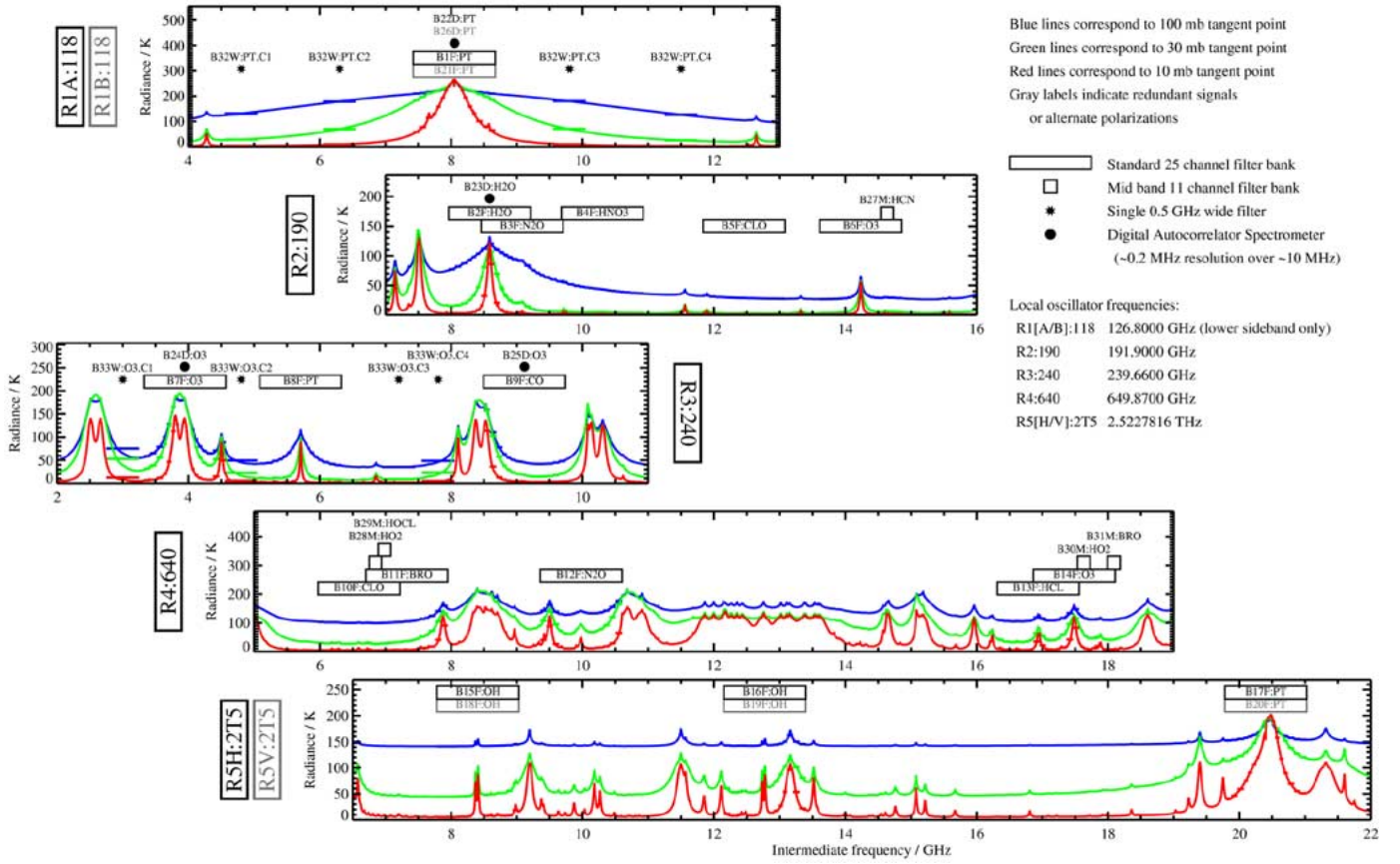
EOS MLS Spectral Coverage

Fig. 1.   Spectral regions measured by EOS MLS and calculated atmospheric signals at three limb tangent pressures. The intermediate frequency scale is relative to the LO frequency and includes signals above and below the LO frequency except R1A and R1B, which only receives frequencies below the LO.

4) *Channel radiance* convolves these radiances with the MLS spectral responses to give radiances in EOS MLS spectral channels.

5) *Antenna radiance* convolves these channel radiances with the MLS antenna FOV.

6) *Combine Sidebands* sums the antenna radiances weighted by their upper and lower sideband fractions.

7) *Scan Motion Radiance* accounts for the vertical smoothing due to the continuous movement of the antenna. This effect is neglected in the current version (v1.51) but will be added in future versions.

8) *Add Baseline* adds a spectrally invariant offset to the radiance.

9) *Scan Residual Model* computes the height of the GHz or THz limb tangent pressure derived from hydrostatic balance.

II. MEASUREMENT DEFINITIONS

A. EOS MLS Calibrated Radiance

Level 1 data processing [3] produces radiances from raw instrument data (Level 0), defined by (1), shown at the bottom of the page, where

$(\overset{\bullet}{I}(\mathbf{x}) - I_{\mathrm{b}l})_{\mathrm{R,c}}$ radiance incident upon the switching mirror, corrected for a "spectral baseline" determined from a combination of modeled extraneous antenna effects [17] and views of "cold space" through the antenna [3];

$\mathbf{x}$ state vector, describing vertical profiles of atmospheric temperature and composition, along with tangent pressure, measurement track tangent angle, and baseline; it is the value of $\mathbf{x}$ that is produced by Level 2 [4];

$$\left(\overset{\bullet}{I}(\mathbf{x}) - I_{\mathrm{b}l}\right)_{\mathrm{R,c}} = \mathrm{BL}_{\mathrm{R},t} + \frac{1}{t_2 - t_1} \int_{t_1}^{t_2} \mathrm{d}t \left\{ r_{\mathrm{u,R,c}} \frac{\int_{\nu_{\mathrm{lo,R}}}^{\infty} \int_{\Omega_A} I(\nu, \mathbf{x}(\Omega)) \Phi_{\mathrm{R,c}}(\nu) G(\Omega, \Omega_t(t), \nu) \mathrm{d}\Omega \, \mathrm{d}\nu}{\int_{\nu_{\mathrm{lo,R}}}^{\infty} \int_{\Omega_A} \Phi_{\mathrm{R,c}}(\nu) G(\Omega, \Omega_t(t), \nu) \, \mathrm{d}\Omega \, \mathrm{d}\nu} \right.$$
$$\left. + r_{\mathrm{l,R,c}} \frac{\int_{-\infty}^{\nu_{\mathrm{lo,R}}} \int_{\Omega_A} I(\nu, \mathbf{x}(\Omega)) \Phi_{\mathrm{R,c}}(\nu) G(\Omega, \Omega_t(t), \nu) \mathrm{d}\Omega \, \mathrm{d}\nu}{\int_{-\infty}^{\nu_{\mathrm{lo,R}}} \int_{\Omega_A} \Phi_{\mathrm{R,c}}(\nu) G(\Omega, \Omega_t(t), \nu) \, \mathrm{d}\Omega \, \mathrm{d}\nu} \right\} \tag{1}$$
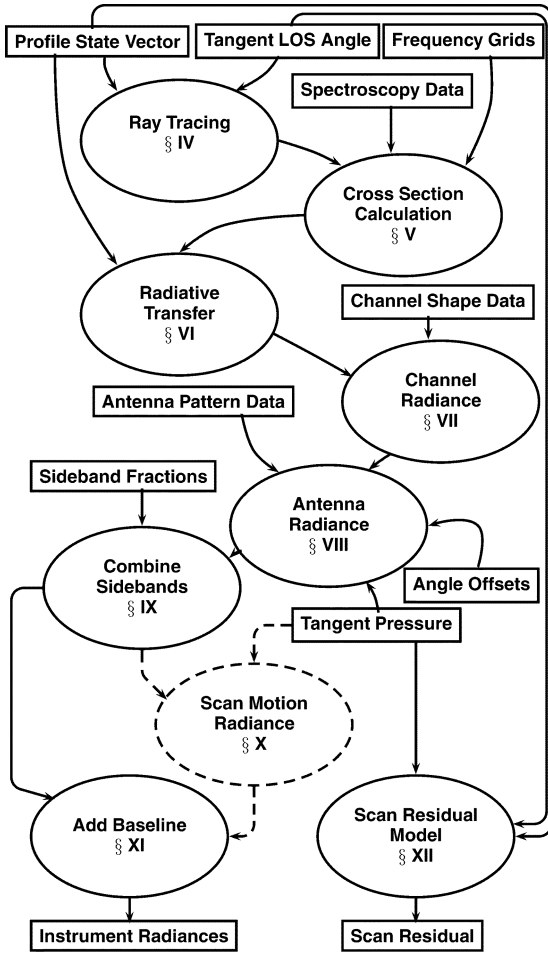
Fig. 2.   EOS MLS forward model schematic.

$BL_{R,t}$	radiometer and tangent-height-dependent additive baseline that is retrieved [4];
$r_{u,R,c}$	upper sideband relative response;
$r_{l,R,c}$	lower sideband relative response;
$\nu_{lo,R}$	local oscillator (LO) frequency;
$I(\nu, \mathbf{x}(\Omega))$	monochromatic, single-ray limb radiance;
$\Phi_{R,c}(\nu)$	instrument spectral response;
$G(\Omega, \Omega_t(t), \nu)$	antenna FOV;
ν	frequency;
Ω	pointing solid angle of the limb radiance LOS;
$\Omega_t(t)$	FOV direction that varies with time during the measurement;
t	time;
Ω_A	portion of solid angle for which the antenna FOV is measured.

The integrals in the denominator of (1) are normalizations of the instrument response functions. The integrated antenna gain over Ω_A (~ 0.4 sr) is slightly less than 4π where $\int_{4\pi} G(\Omega, \Omega_t(t), \nu)d\Omega = 4\pi$. A correction for the radiance outside ~ 0.4 sr is included in I_{bl} [17]. Quantities that are sideband, radiometer, channel, and FOV pointing direction dependent are designated with subscripts, s = u or l, for sideband; R = R1A, R1B, R2, R3, R4, R5H, or R5V for radiometer; c for channel; and t for limb tangent height.

The sideband fractions $r_{u,R,c}$ and $r_{l,R,c}$ describe the radiometer's relative response in its upper and lower sidebands, and include signal loss through the antenna system as a consequence of scattering, spill-over, and absorption [17]. The sideband fractions $r_{u,R,c}$ and $r_{l,R,c}$ are given by

$$r_{u,R,c} = \eta_{u,R,c}^A \rho_R^A r'_{u,R,c}$$

$$r_{l,R,c} = \eta_{l,R,c}^A \rho_R^A r'_{l,R,c}$$

$$r'_{u,R,c} = \frac{\eta_{u,R,c}^A r''_{u,R,c}}{\eta_{u,R,c}^A r''_{u,R,c} + \eta_{l,R,c}^A r''_{u,R,c}}$$

$$r'_{l,R,c} = \frac{\eta_{l,R,c}^A r''_{l,R,c}}{\eta_{u,R,c}^A r''_{u,R,c} + \eta_{l,R,c}^A r''_{l,R,c}}$$

$$r''_{u,R,c} = \frac{\int_{\nu_{lo,R}}^{\infty} \Phi_{R,c}(\nu)\, d\nu}{\int_{-\infty}^{\infty} \Phi_{R,c}(\nu)\, d\nu}$$

$$r''_{l,R,c} = \frac{\int_{-\infty}^{\nu_{lo,R}} \Phi_{R,c}(\nu)\, d\nu}{\int_{-\infty}^{\infty} \Phi_{R,c}(\nu)\, d\nu} \tag{2}$$

where $\eta_{l,R,c}^A$ and $\eta_{u,R,c}^A$ are the antenna efficiencies for the lower and upper frequency sidebands, and ρ_R^A (same for both sidebands) is the product of the reflectivities of the antenna system. The spectral response function, $\Phi_{R,c}$, has responses at frequencies above and below the LO frequency. The 118-GHz radiometer is an exception having a response only in the lower sideband. The switching mirror for the THz instrument is in front of its antenna, and thus its losses are calibrated out [18], giving $r_{u,R,c} = r''_{u,R,c}$, $r_{l,R,c} = r''_{l,R,c}$, and $I_{bl} = 0$.

B. Level 1 GHz and THz Tangent Angles and Heights

The Aura flight operations team provides the spacecraft location, attitude, and velocity. The EOS MLS GHz antenna and THz switching mirror encoders give the angular positions of their FOV directions. From these, the limb tangent angles along the measurement great circle arc and tangent heights of the GHz and THz FOV directions are determined. The measurement track tangent angle are used by the ray tracing calculation. The spacecraft velocity projected onto the ray traced LOS is used for Doppler shifting the molecular lines measured by EOS MLS. The height measurements (Level 1 GHz and THz pointing tangent heights) are used in the scan residual model to retrieve tangent pressure and temperature as described in [4, Sec. III-E].

C. State Vector

The state vector $\mathbf{x}$ consists of the independent variables being retrieved. It is composed of two variable types, $\vec{x}_t$, and $\mathbf{f}$. The variable type, $\vec{x}_t$, consists of quantities that are retrieved for every MLS 1/6-s measurement, for example the limb tangent pressure, and $BL_{R,t}$ in (1). The second variable type, the representation state vector, $\mathbf{f}$, has values at specified pressures and measurement track angles. Temperature and molecular composition are components of $\mathbf{f}$.

III. ATMOSPHERIC REPRESENTATION

The atmosphere is represented by a series of vertical profiles along the measurement track. The measurement track coordi-
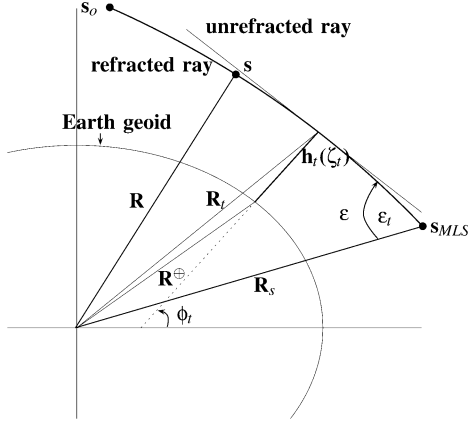
Fig. 3. Variables used in relation to the Earth geoid projected onto the measurement track angle line-of-sight frame.

nate is ϕ, the geodetic great circle angle along the measurement track, between the equator and the location of the vertical profile. The vertical coordinate of the profiles is $\zeta = -\log(P)$ where P is atmospheric pressure in hPa. The EOS MLS atmospheric representation for the kth state vector component are functions of the form

$$\mathbf{f}^k(\zeta, \phi) = \sum_l^{NH^k} \sum_m^{NP^k} f_{lm}^k \eta_l^k(\zeta) \eta_m^k(\phi) \tag{3}$$

$$\mathbf{f}^k(\zeta, \phi) = \exp\left[\sum_l^{NH^k} \sum_m^{NP^k} \ln f_{lm}^k \eta_l^k(\zeta) \eta_m^k(\phi) \right] \tag{4}$$

where $\mathbf{f}^k(\zeta, \phi)$ is the continuous representation, f_{lm}^k are its values at breakpoints l and m, each representing a vertical and angular value, NH^k and NP^k are the total number of vertical and angular breakpoints respectively. The linear function (3) is used for all species except H_2O because it permits retrieved profile fluctuations about zero concentration which is needed in order to not introduce a positive bias in averages of individual measurements with low signal-to-noise. The logarithmic function, (4), is used for H_2O because the exponential shape more closely models its steep vertical gradient in the troposphere and the H_2O signal-to-noise is very high. The functions $\eta_l^k(\zeta)$ and $\eta_m^k(\phi)$, represent a piecewise-linear interpolation.

The v1.51 EOS MLS constituent curtain consists of profiles having six vertical breakpoints every decade change in pressure from 10^3–10^{-1} hPa and 3 levels per decade change in pressure from 10^{-1}–10^{-5} hPa, separated every 1.5° along the measurement track angle [4].

IV. RAY TRACING

The first task in the radiative transfer calculation is determining the atmospheric state at selected points along the MLS LOS. These points serve as the quadrature for solving the radiative transfer equation. Fig. 3 shows one ray. This ray is shown in the LOS frame (LOSF) coordinate system. The x-y axes of the LOSF are the Aura orbital plane (neglecting small instrument pointing misalignments). The Earth geoid is a surface of constant geopotential (62.636 81 km$^2 \cdot$ sec^{-2} [19]). The LOS ray, s, is characterized by its tangent pressure, ζ_t, and tangent

geodetic angle along the measurement track great circle arc, ϕ_t. Both the tangent pressure and tangent geodetic angle include the effect of refractive bending. The height, h_t, is dependent on the tangent pressure according to hydrostatic balance. The tangent pressure is the point on s whose height is both normal to the Earth geoid and s. The tangent pressure and tangent geodetic angle provide the vertical and horizontal location from which to evaluate the atmospheric state along the ray trace.

The breakpoint pressures of the piecewise-linear representation determine where the atmospheric state is evaluated along s. These pressures also establish the tangent heights of the LOS rays to be computed. We double the number of grid points in the troposphere and lower stratosphere to more accurately account for vertical structure. This is the preselected integration grid (PSIG), which is used for solving the radiative transfer equation.

A. Hydrostatic Model

The atmosphere is assumed to be in hydrostatic balance which allows calculation of heights from pressure and temperature according to [8]

$$h\left(\zeta, \phi_m^T\right) = \frac{g_o \overset{\star}{R}_o^2}{g_o \overset{\star}{R}_o - k \ln 10 \sum_l^{NH^T} \sum_m^{NP^T} \left(f_{lm}^T \eta_m^T \left(\phi_m^T\right) P_l\right)} - \overset{\star \oplus}{R} \tag{5}$$

where k, is the Boltzmann constant, P_l is the integral

$$P_l = \int_{\zeta_o}^{\zeta} \frac{\eta_l^T(\zeta)}{\mathcal{M}(\zeta)} d\zeta \tag{6}$$

$\mathcal{M}$ is mean molecular mass, ζ_o is the negative logarithm of pressure at height h_o, g_o is the gravitational acceleration at h_o, $\overset{\star \oplus}{R}$ is the effective Earth radius and $\overset{\star}{R}_o = \overset{\star \oplus}{R} + h_o$. Expressions for g_o and $\overset{\star \oplus}{R}$ are given in [8] and [20]. Equation (5) embeds the piecewise-linear temperature function into the hydrostatic calculation. A 2–D (angle and pressure) array of heights are produced from (5) at the temperature measurement track angles and the PSIG pressures. Using an iterative procedure described in [8], the LOS angles corresponding to the PSIG pressures and the FOV direction measurement track tangent angle are determined. The atmospheric constituent values along the LOS are readily evaluated with (3) or (4).

The temperature Jacobian of (5) is

$$\frac{\partial h}{\partial f_{lm}^T} = \frac{g_o k \ln 10 \overset{\star}{R}_o^2 \eta_m^T \left(\phi_m^T\right) P_l}{\left[g_o \overset{\star}{R}_o - k \ln 10 \sum_l^{NH^T} \sum_m^{NP^T} \left(f_{lm}^T \eta_m^T \left(\phi_m^T\right) P_l\right)\right]^2} \tag{7}$$

where the T superscript denotes terms pertaining to the temperature components of the state vector. The LOS ray traced $\partial R / \partial f_{lm}^T$ used in the radiative transfer and FOV Jacobian calculations is interpolated from the $\partial h / \partial f_{lm}^T$s.

V. SPECTROSCOPY

A. Molecules Considered

The EOS MLS bands (see Fig. 1) are affected by signals from many molecules. Table I lists the molecules including

TABLE I
MOLECULES WHOSE LINES WERE SCANNED FOR INCLUSION IN THE EOS MLS FORWARD MODEL

^{79}BrO	$^{79}BrO(v_1)$	^{81}BrO	$^{81}BrO(v_1)$	CH_3CN	CH_3COCH_3	CH_3Cl	$CH_3^{35}Cl$	$CH_3^{37}Cl$	CH_3OH	CO	^{13}CO
$C^{17}O$	$C^{18}O$	$OC^{18}O$	^{35}ClO	$^{35}ClO(v_1)$	^{37}ClO	$^{37}ClO(v_1)$	COF_2	$^{35}ClOO^{35}Cl$	$^{35}ClOO^{37}Cl$	$^{35}ClONO_2$	$^{37}ClONO_2$
$H^{79}Br$	$H^{81}Br$	$H^{35}Cl$	$H^{37}Cl$	$D^{35}Cl$	$D^{37}Cl$	HCN	$HCN(v_2)$	$H^{13}CN$	$HC^{15}N$	$HCOOH$	HF
DF	H_2CO	$H_2^{13}CO$	$H_2C^{18}O$	H_2O	$H_2O(v_2)$	$H_2^{17}O$	$H_2^{17}O(v_2)$	$H_2^{18}O$	$H_2^{18}O(v_2)$	D_2O	HDO
$HDO(v_2)$	$HD^{17}O$	$HD^{18}O$	H_2O_2	$H_2^{32}S$	$H_2^{32}SO_4$	HNO_3	$HNO_3(v_5)$	$HNO_3(v_6)$	$HNO_3(v_7)$	$HNO_3(v_8)$	$HNO_3(v_9)$
$HO^{79}Br$	$HO^{81}Br$	$HO^{35}Cl$	$HO^{37}Cl$	HO_2	$HOONO_2$	N_2	N_2O	$N_2O(v_1)$	$N_2O(v_2)$	$N_2O(2v_2)$	^{15}NNO
$N^{15}NO$	$N_2^{17}O$	$N_2^{18}O$	NO	NO_2	O	^{17}O	^{18}O	$O^{35}ClO$	$O^{37}ClO$	$OC^{32}S$	$OC^{34}S$
$O^{13}C^{32}S$	OH	^{18}OH	OD	O_2	$O_2(v_1)$	$O^{17}O$	$O^{18}O$	$O^{18}O(v_1)$	$^1\Delta_g O_2$	$^1\Delta_g^{18}OO$	O_3
$O_3(v_{1,3})$	$O_3(v_2)$	$O_3(2v_2)$	$O_3(v_{1,3}+v_2)$	$O_2^{17}O$	$O^{17}OO$	$O_2^{18}O$	$O_2^{18}O(v_2)$	$O^{18}OO$	$O^{18}OO(v_2)$	$^{32}SO_2$	$^{32}SO_2(v_2)$
$^{33}SO_2$	$^{34}SO_2$										

vibrational states and isotopes whose lines have been scanned for inclusion in the MLS forward model. Frequencies and line strengths of these molecules are taken from the JPL Spectroscopy Catalog [21] or the HITRAN database [22].

B. EOS MLS Molecular Line Catalog

The EOS MLS molecular line catalog consists of two parts: 1) molecule data and 2) line data. The molecule data includes the isotopic abundance, mass, partition function values, and line shape continuum parameters. The isotopic abundances are based on crustal values of the elements except for ^{18}OO which is based on atmospheric measurements [23]. The isotopic abundances are used to scale the molecular concentrations to its isotopic concentrations. The partition function includes all known rotation, vibration and electronic energy levels for the molecule. The continuum parameters are used to model measured absorption unaccounted for by the line by line (LBL) model and wing absorption from strong distant lines that are more simply modeled with a pressure-squared and frequency-squared continuum function. Continuum absorption measurements for air and H_2O for the 170–260-GHz range are from [24] and H_2O near 2.5 THz are from [25]. Air and H_2O continua for 114–123 GHz and 620–660 GHz are from [26]. In-orbit data are used to characterize the O_3 continuum. The 640-GHz (R4) radiometer showed unusually large baseline signatures in early retrievals, which correlated very well measured O_3 concentrations. These baseline signatures were later used to infer an O_3 continuum function. Adding the in-orbit derived O_3 continuum has significantly reduced the baseline signatures for R4. This procedure was repeated for R2 and R3. We have defined a fictitious continuum species, EXTINCTION that allows Level 2 to retrieve excess absorption [4].

The EOS MLS catalog includes all lines and continua of N_2, O_2, H_2O, and O_3 from 0 to 3 THz having an estimated strength (line plus continuum) greater than 1 K at their line centers. Other molecular lines including weaker lines from O_2, H_2O, and O_3 are individually selected for each EOS MLS band when its estimated optically thin radiance exceeds a threshold (1 K for R1A, R1B, and R3, 0.5 K for R5 V and R5H, and 0.05 K for R2 and R4). The JPL and HITRAN databases are searched over the full EOS MLS spectral coverage of a band or a group of overlapping bands (from the lowest frequency channel minus one half its band width to the highest frequency channel plus one half its bandwidth) plus or minus an additional 520 MHz which is

where a Lorentz becomes 1/4 of its maximum at 100 hPa, a rough approximation to where we enter the ν^2 continuum limit. Any molecule listed in Table I having a line inside the frequency window with an estimated strength greater than that threshold is included in the EOS MLS catalog. The complete tables are in [8].

C. Cross Sections

The cross section (absorption coefficient divided by mixing ratio), β^k, for the kth molecule is given by

$$\beta^k = \beta^k_{LBL} + \beta^k_{cont} \tag{8}$$

where β^k_{LBL} is the LBL contribution and β^k_{cont} is the continuum contribution. The expression for the LBL cross section is given in [8], [7], and [12]. We use a Voigt lineshape with a Van Vleck-Huber prefactor [12], [27]. Molecular line positions are pressure shifted and Doppler blue-shifted to account for the orbital motion.

Derivatives of β^k with respect to temperature, line broadening, and line position are needed for computing radiance Jacobians. Analytic expressions for these are in [8].

VI. RADIATIVE TRANSFER

The unpolarized radiative transfer equation for a nonscattering atmosphere in local thermodynamic equilibrium is [28]

$$\frac{dI(\nu, \mathbf{x}(s))}{ds} + \kappa(\nu, \mathbf{x}(s))I(\nu, \mathbf{x}(s)) = \kappa(\nu, \mathbf{x}(s))B(\nu, \mathbf{x}(s)) \tag{9}$$

where $\kappa(\nu, \mathbf{x}(s)) = \sum_k f^k \beta^k$ is the atmospheric absorption coefficient and $B(\nu, \mathbf{x}(s))$ is the source function. Equation (9) can be rewritten as [12], [28]

$$I(\nu, \mathbf{x}(s_{MLS})) = I(\nu, \mathbf{x}(s_o))\mathcal{T}(\nu, \mathbf{x}(s_{MLS}))$$
$$+ \int_{s_o}^{s_{MLS}} B(\nu, \mathbf{x}(s))\kappa(\nu, \mathbf{x}(s))\mathcal{T}(\nu, \mathbf{x}(s))\,ds \tag{10}$$

where $s = s_o$ and $s = s_{MLS}$ are the path locations at the top of the atmosphere and at the EOS MLS respectively (Fig. 3) and $\mathcal{T}(\nu, \mathbf{x}(s))$ is the atmospheric transmissivity defined as

$$\mathcal{T}(\nu, \mathbf{x}(s)) = \exp\left(-\int_{s_o}^s \kappa(\nu, \mathbf{x}(s'))\,ds'\right). \tag{11}$$

Recognizing that $d\mathcal{T} = -\kappa\mathcal{T}ds$ and integrating by parts (11) rearranges to

$$
\begin{aligned}
I(\nu, \mathbf{x}(s_{\text{MLS}})) = &(I(\nu, \mathbf{x}(s_o)) - B(\nu, \mathbf{x}(s_o)))\mathcal{T}(\nu, \mathbf{x}(s_{\text{MLS}})) \\
&+ B(\nu, \mathbf{x}(s_{\text{MLS}})) - \int_{B(\nu, \mathbf{x}(s_o))}^{B(\nu, \mathbf{x}(s_{\text{MLS}}))} \mathcal{T}(\nu, \mathbf{x}(s)) \\
&\times dB(\nu, \mathbf{x}(s)).
\end{aligned}
\tag{12}
$$

A. Discrete Radiative Transfer Equation

The discrete form of (12) using the layer notation in [7, Fig. 3] is

$$
I(\nu, \mathbf{x}(\epsilon)) = \sum_{i=1}^{t} \Delta B_i \mathcal{T}_i + \sum_{i=2N-t+1}^{2N} \Delta B_i \mathcal{T}_i
\tag{13}
$$

where ϵ is the refracted pointing angle of the LOS ray trace, t is the tangent level, $i = 1$ is the path point nearest to MLS, and ΔB_i is the differential source function given by

$$
\Delta B_i = \frac{B_{i+1} - B_{i-1}}{2}
\tag{14}
$$

with special cases for the top of the atmosphere and the tangent level

$$
\begin{aligned}
\Delta B_1 &= \frac{B_1 + B_2}{2} \\
\Delta B_t &= \frac{B_{2N-t+1} - B_{t-1}}{2} \\
\Delta B_{2N-t+1} &= \frac{B_{2N-t+2} - B_t}{2} \\
\Delta B_{2N} &= I_o - \frac{B_{2N-1} + B_{2N}}{2}.
\end{aligned}
\tag{15}
$$

$I_o(= I(\nu, \mathbf{x}(0)))$ is the background cosmic radiance incident on the atmosphere, B is the Planck radiation function expressed in temperature units [28]

$$
B_i = \frac{h\nu}{k\left[\exp\left(\frac{h\nu}{kT_i}\right) - 1\right]}
\tag{16}
$$

h is Planck's constant, k is Boltzmann's constant, ν is the radiation frequency and T_i is temperature at the ith level. $\mathcal{T}_i$ is the transmissivity from the ith level to the EOS MLS given by

$$
\begin{aligned}
\mathcal{T}_1 &= 1, && \text{for } 1 < i \leq t \\
\mathcal{T}_i &= \exp\left(-\sum_{j=2}^{i} \Delta\delta_{j\to j-1}\right), && \text{for } i = 2N-t+1 \\
\mathcal{T}_{2N-t+1} &= \Upsilon\mathcal{T}_t, && \text{for } i > 2N-t+1 \\
\mathcal{T}_i &= \mathcal{T}_{2N-t+1}\exp\left(-\sum_{j=2N-t+2}^{i} \Delta\delta_{j-1\to j}\right) && (17)
\end{aligned}
$$

where $\Delta\delta_{j\to j-1}$ is the incremental opacity between levels j and $j-1$, and Υ is the Earth surface reflectivity. The limits for the incremental opacity integral are reversed for $i > t$ to keep the lower limit closest to the tangent surface. The Earth reflectivity is 1 for all limb tangents above the Earth's surface. In limb viewing, the atmosphere is usually not transmissive enough to see the surface. We use $\Upsilon = 0.05$ and set the reflection boundary occurring at the reference geopotential. Variations in

Υ and surface topography are not considered. This simplification may cause errors over high mountains or where the atmosphere is very dry over Antarctica. Radiance data collected thus far does reveal computational errors of several 10 s of K for limb tangents greater than 700 hPa over Antarctica having an elevation greater than 3 km. Evidence of computational errors caused by this approximation over high mountains such as the Tibetan Plateau is inconclusive. The atmosphere over these mountains is considerably moister than over Antarctica and often cloudy limiting the penetration depth of MLS.

The incremental opacity is given by

$$
\Delta\delta_{i\to i-1} = \sum_{k=1}^{NS} \Delta\delta_{i\to i-1}^k
\tag{18}
$$

where k is a molecule and NS is the total number of molecules considered. The species incremental opacity integral is

$$
\Delta\delta_{i\to i-1}^k = \frac{\Delta s_{i\to i-1}^{\text{refr}}}{\Delta s_{i\to i-1}} \int_{\zeta_i}^{\zeta_{i-1}} \mathsf{f}^k(\zeta, \phi(\zeta))\beta^k \frac{ds}{dh}\frac{\partial h}{\partial \zeta}d\zeta
\tag{19}
$$

where f^k is either from (3) or (4) and β^k is the cross section for the kth molecule. ζ is the LOS path coordinate; it establishes h and ϕ as described in Section IV. Refraction causes a path-lengthening effect relative to the unrefracted path lengths used here. This is compensated for by scaling the opacity integral by the ratio of the unrefracted path length to the refracted one. Numerical experiments have shown this to be a satisfactory approximation (<0.01 K). The path length ratio is given by

$$
\frac{\Delta s_{i\to i-1}^{\text{refr}}}{\Delta s_{i\to i-1}} = \int_{\zeta_i}^{\zeta_{i-1}} \frac{\mathcal{N}R}{\sqrt{\mathcal{N}^2 R^2 - \mathcal{N}_t^2 R_t^2}}\frac{\partial h}{\partial \zeta}d\zeta \bigg/ \int_{\zeta_i}^{\zeta_{i-1}} \frac{ds}{dh}\frac{\partial h}{\partial \zeta}d\zeta
\tag{20}
$$

where $\mathcal{N}$ is the refractive index

$$
\mathcal{N} = 1 + \frac{0.0000776}{T(\zeta, \phi)10^\zeta}\left(1 + 4810\frac{\mathsf{f}^{\text{H2O}}(\zeta, \phi)}{T(\zeta, \phi)}\right).
\tag{21}
$$

The integrals in (19) are solved semi-adaptively using either a three-point Gauss–Legendre quadrature with singular-value elimination or with a rectangular quadrature as described in [8].

B. Discrete Radiative Transfer Jacobians

The Jacobian of (13) is

$$
\frac{\partial I(\nu, \mathbf{x}(\epsilon))}{\partial x_j} = \sum_{i=1}^{t} \mathcal{Q}_i \mathcal{T}_i + \sum_{i=2N-t+1}^{2N} \mathcal{Q}_i \mathcal{T}_i
\tag{22}
$$

where x_j is an element in state vector ($\mathbf{x}$) and

$$
\mathcal{Q}_i = \frac{\partial \Delta B_i}{\partial x_j} - \Delta B_i \mathcal{W}_i
\tag{23}
$$

where $\mathcal{W}_i$ is the transmittance derivative given by

$$
\begin{aligned}
\mathcal{W}_1 &= 0, && \text{for } i \leq t \\
\mathcal{W}_i &= \mathcal{W}_{i-1} + \frac{\partial \Delta\delta_{i\to i-1}}{\partial x_j}, && \text{for } i = 2N-t+1 \\
\mathcal{W}_{2N-t+1} &= \mathcal{W}_t, && \text{for } i > 2N-t+1 \\
\mathcal{W}_i &= \mathcal{W}_{i-1} + \frac{\partial \Delta\delta_{i-1\to i}}{x_j} && (24)
\end{aligned}
$$

where $\partial\Delta\delta_{i\to i-1}/\partial x_j$ is the layer opacity Jacobian with respect to state vector element x_j.
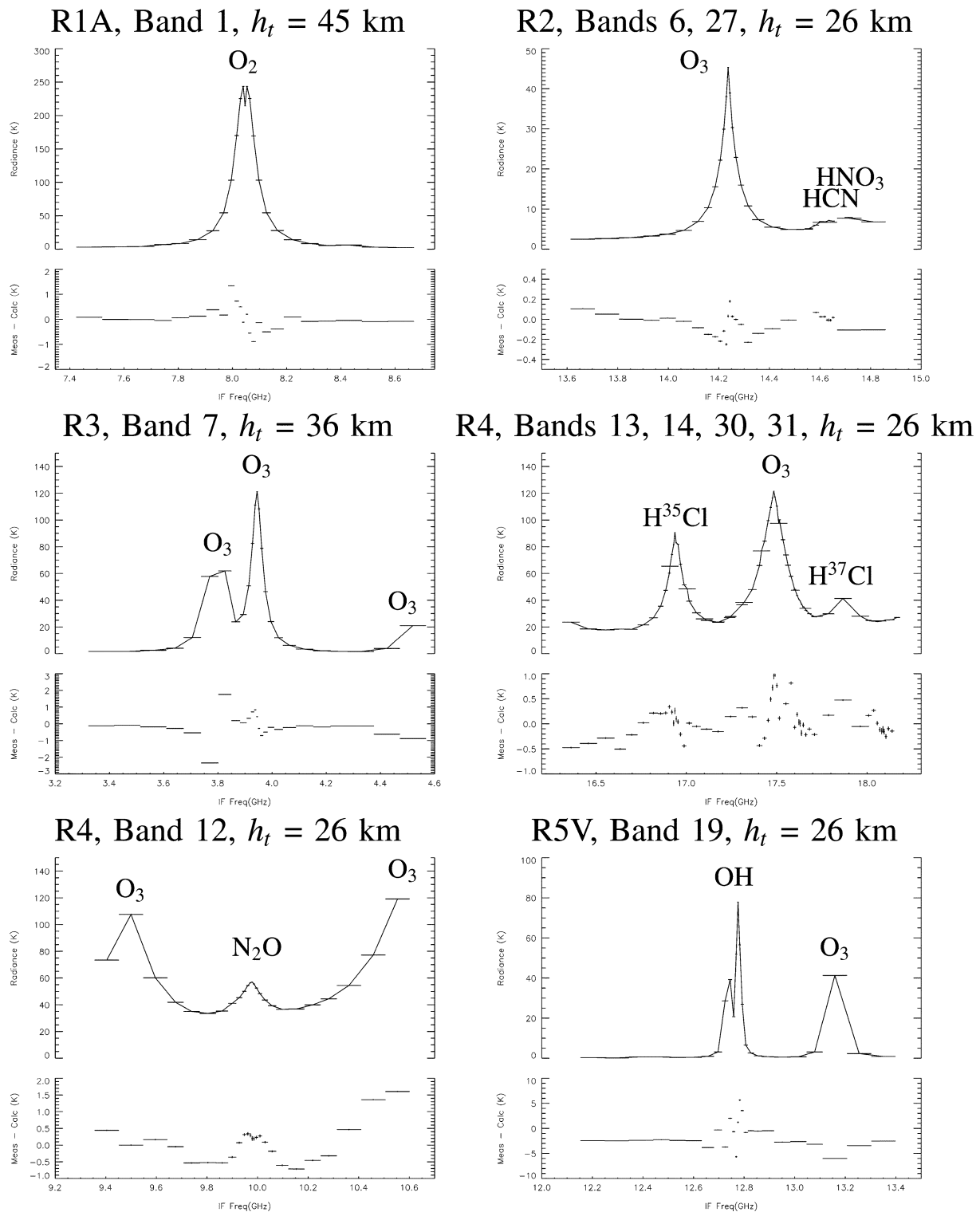
Fig. 4.   Examples of radiance spectra measured by the EOS MLS radiometers in six spectral regions as indicated. The upper plot shows the measured spectrum which is a daily average of measurements on June 29, 2005 for a single integration period that points approximately to the height shown. The lower plot shows the daily average of the difference spectrum, or residual, between measured and calculated radiances using the retrieved state vector. Each EOS MLS channel is represented by a + whose horizontal width indicates its spectral bandwidth, and the height of the vertical bar is the precision of the average, which is the individual measurement precision reduced by the square root of the number of samples averaged. The excessive averaging makes the precision bar for many channels smaller than the thickness of the channel bandwidth line. A line joining the channel centers is overlaid on each measured spectra. See text for an explanation of the missing channels in the residual spectrum.

C. Opacity and Source Function Jacobians

The radiative transfer Jacobian in (22) is a function of the opacity Jacobian and the differential source function Jacobian.

We now consider Jacobians for species mixing ratio, temperature, and cross-section terms separately.

1) Mixing Ratio: The source function Jacobian with respect to mixing ratio is zero. The opacity Jacobian with respect to

mixing ratio for the linear basis is

$$
\frac{\partial \Delta \delta_{i \to i-1}^k}{\partial f_{lmn}^k} = \frac{\Delta s_{i \to i-1}^{\text{refr}}}{\Delta s_{i \to i-1}} \int_{\zeta_i}^{\zeta_{i-1}} \eta_l^k(\zeta) \eta_m^k(\phi(\zeta)) \beta^k \frac{\mathrm{d}s}{\mathrm{d}h} \frac{\partial h}{\partial \zeta} \mathrm{d}\zeta.
$$
(25)

The opacity Jacobian with respect to mixing ratio for the logarithmic basis is

$$
\frac{\partial \Delta \delta_{i \to i-1}^k}{\partial f_{lmn}^k} = \frac{\Delta s_{i \to i-1}^{\text{refr}}}{\Delta s_{i \to i-1}} \int_{\zeta_i}^{\zeta_{i-1}} \frac{\eta_l^k(\zeta) \eta_m^k(\phi(\zeta))}{f_{lmn}^k}
$$
$$
\times \mathsf{f}^k(\zeta, \phi(\zeta)) \beta^k \frac{\mathrm{d}s}{\mathrm{d}h} \frac{\partial h}{\partial \zeta} \mathrm{d}\zeta. \quad (26)
$$

The logarithmic representation requires $f_{lmn}^k > 0$.

2) Temperature: The Jacobian for temperature must include its effect on absorption, pathlength between pressure grid points on the LOS and the source function. The change in the ratio of the refracted to unrefracted path lengths due to temperature is ignored. Substituting $\mathrm{d}s/\mathrm{d}h = R/\sqrt{R^2 - R_t^2}$ into (19) and differentiating with respect to f_{lmn}^T gives [8]

$$
\frac{\partial \Delta \delta_{i \to i-1}^k}{\partial f_{lmn}^T} \approx \frac{\Delta s_{i \to i-1}^{\text{refr}}}{\Delta s_{i \to i-1}} \int_{\zeta_i}^{\zeta_{i-1}} \mathrm{d}\zeta
$$
$$
\times \left\{ \mathsf{f}^k \frac{\partial \beta^k}{\partial T} \frac{\eta_l^T(\zeta) \eta_m^T(\phi(\zeta))}{T} \frac{\mathrm{d}s}{\mathrm{d}h} \frac{\partial h}{\partial \zeta} \right.
$$
$$
+ \mathsf{f}^k \beta^k \frac{2R^2 \frac{\partial R}{\partial f_{lm}^T} - 3R_t^2 \frac{\partial R}{\partial f_{lm}^T} + R R_t \frac{\partial R_t}{\partial f_{lm}^T}}{(R^2 - R_t^2)^{\frac{3}{2}}} \frac{\partial h}{\partial \zeta}
$$
$$
\left. + \mathsf{f}^k \beta^k \frac{\eta_l^T(\zeta) \eta_m^T(\phi(\zeta))}{T} \frac{\mathrm{d}s}{\mathrm{d}h} \frac{\partial h}{\partial \zeta} \right\}.
$$
(27)

The first term in (27) is the temperature sensitivity of the cross section, and the second two terms are the temperature sensitivity to the path length between pressures.

The source function Jacobian $\mathrm{d}\Delta B_i/\mathrm{d}T_{lm}$ for temperature is

$$
\frac{\mathrm{d}\Delta B_i}{\mathrm{d}T_{lm}} = \frac{\frac{\mathrm{d}B_{i+1}}{\mathrm{d}T_{lm}} - \frac{\mathrm{d}B_{i-1}}{\mathrm{d}T_{lm}}}{2}
$$

where

$$
\frac{\partial B_i}{\partial T_{lm}} = \frac{B_i^2 \exp\left\{\frac{\mathsf{h}\nu}{\mathsf{k}T_i}\right\}}{T_i^2} \eta_l^T(\zeta_i) \eta_m^T(\phi(\zeta_i)). \quad (28)
$$

3) Cross-Section Jacobians: The cross-section Jacobians pertain to those state vector components (except temperature) that affect the species cross section. These include spectroscopic parameters such as the broadening parameter, the line broadening temperature dependence, and line position. Radiance sensitivities to β are given by

$$
\frac{\partial \Delta \delta_{i \to i-1}^k}{\partial x_j} = \frac{\Delta s_{i \to i-1}^{\text{refr}}}{\Delta s_{i \to i-1}} \int_{\zeta_i}^{\zeta_{i-1}} \mathsf{f}^k \frac{\partial \beta^k}{\partial x_j} \frac{\mathrm{d}s}{\mathrm{d}h} \frac{\partial h}{\partial \zeta} \mathrm{d}\zeta. \quad (29)
$$

VII. Channel Radiance

The EOS MLS channels measure radiation averaged over a finite spectral bandwidth. The methodology for computing the spectral integral in (1) is described here.

A. Filter Bank Channels

The upper sideband radiance for each channel and tangent height is

$$
I_{\mathrm{u,R,c}}(\mathbf{x}(\epsilon)) = \frac{\int_{\nu_{\mathrm{lo,R}}}^{\infty} I(\nu, \mathbf{x}(\epsilon)) \Phi_{\mathrm{R,c}}(\nu) \, \mathrm{d}\nu}{\int_{\nu_{\mathrm{lo,R}}}^{\infty} \Phi_{\mathrm{R,c}}(\nu) \, \mathrm{d}\nu}. \quad (30)
$$

There is a similar equation for the lower sideband [see (1)]. The radiances $I(\nu, \mathbf{x}(\epsilon))$ are evaluated on an optimized frequency quadrature ("Frequency grids" in Fig. 2) that has a higher density of points where the spectral radiance gradient is greater. Each tangent pressure has its own quadrature to accommodate different linewidths. The channel spectral response, $\Phi_{\mathrm{R,c}}(\nu)$, is given on a fine frequency grid ("Channel shape data" in Fig. 2). The computed radiances on the optimized quadrature are interpolated to this grid and (30) is evaluated with a trapezoid rule. The channel radiance Jacobians are evaluated similarly.

B. DACS

Digital autocorrelator spectrometers (DACS) resolve narrow-line, Doppler-broadened emission from the mesosphere and lower thermosphere with 129 channels equally spaced across 12.5 MHz. Since all the DACS channels have identical filter shapes it is more efficient to use the Fourier transform convolution theorem to evaluate (30). The details are given in [29].

VIII. Antenna Radiance

Next we compute antenna radiances from the channel radiances. The angular integration in (1) is [30]

$$
I_{\mathrm{s,R,c}}(\mathbf{x}(\epsilon_t, \alpha_t)) = \mathrm{Tr} \int_{\alpha_A} \int_{\epsilon_A} \mathbf{I}_{\mathrm{s,R,c}}(\mathbf{x}(\epsilon, \alpha))
$$
$$
\times \mathbf{G}_{\mathrm{s,R,c}}(\epsilon_t - \epsilon, \alpha_t - \alpha) \cos \epsilon \, \mathrm{d}\epsilon \, \mathrm{d}\alpha
$$
$$
/ \mathrm{Tr} \int_{\alpha_A} \int_{\epsilon_A} \mathbf{G}_{\mathrm{s,R,c}}(\epsilon_t - \epsilon, \alpha_t - \alpha) \cos \epsilon \, \mathrm{d}\epsilon \, \mathrm{d}\alpha
$$
(31)

where $\mathbf{G}_{\mathrm{s,R,c}}(\epsilon_t - \epsilon, \alpha_t - \alpha)$ is the polarized far-field antenna pattern, Tr is the trace of a matrix, $\mathbf{I}_{\mathrm{s,R,c}}(\mathbf{x}(\epsilon, \alpha))$, the channel-averaged radiance in coherency matrix format [31], angles ϵ and α are elevation (vertical) and azimuth (cross-track) angular components of solid angle, Ω, and α_A and ϵ_A are a portion of the total solid angle Ω for which $\mathbf{G}_{\mathrm{s,R,c}}(\epsilon_t - \epsilon, \alpha_t - \alpha)$ has been measured. For unpolarized radiation, $\mathbf{I}_{\mathrm{s,R,c}}(\mathbf{x}(\epsilon, \alpha))$ is diagonal and the $\mathrm{Tr}\mathbf{G}_{\mathrm{s,R,c}}(\epsilon_t - \epsilon, \alpha_t - \alpha)$ is the sum of the co- and cross-polarized antenna gain patterns. Equation (31) is simplified further by collapsing it to a one-dimensional (1-D) integral given by

$$
I_{\mathrm{s,R,c}}(\mathbf{x}(\epsilon_t)) = \int_{-\infty}^{\infty} I_{\mathrm{s,R,c}}(\mathbf{x}(\epsilon)) \bar{G}_{\mathrm{s,R,c}}(\epsilon_t - \epsilon) \, \mathrm{d}\epsilon \quad (32)
$$

where $I_{\mathrm{s,R,c}}(\mathbf{x}(\epsilon))$ is the channel-averaged radiance (Section VII), $\bar{G}_{\mathrm{s,R,c}}(\epsilon_t - \epsilon)$ is $\mathrm{Tr}\mathbf{G}_{\mathrm{s,R,c}}(\epsilon_t - \epsilon, \alpha_t - \alpha)$ collapsed into the LOSF scan dimension and normalized to unit area,

and ϵ_t is the refracted pointing angle in the LOSF (Fig. 3). The refracted pointing angle is

$$\sin \epsilon_t = \mathcal{N}_t \frac{R_t}{R_s} \tag{33}$$

where R_s and R_t are the spacecraft and LOS tangent height distance to the center of the Earth, respectively. Approximating $\sin(\epsilon_t - \epsilon) \approx \epsilon_t - \epsilon$ allows evaluation of (32) with Fourier transforms

$$\mathcal{F}t(I_{\mathrm{s,R,c}}(\mathbf{x}(\epsilon_t))) = \mathcal{F}t(I_{\mathrm{s,R,c}}(\mathbf{x}(\epsilon))) \times \mathcal{F}t(\bar{G}_{\mathrm{s,R,c}}(\epsilon - \epsilon_t)) \tag{34}$$

where $\mathcal{F}t$ is the Fourier transform.

The antenna radiance Jacobian considers the sensitivity of the antenna radiance to a state vector element at a fixed tangent pressure. Therefore, the antenna radiance Jacobian will include the impact of how the state vector element may change the antenna's half power beam width (HPBW) in tangent pressure coordinates. The antenna radiance Jacobian is given by

$$\begin{aligned}
\frac{\partial I_{\mathrm{s,R,c}}(\mathbf{x}(\epsilon_t))}{\partial x_j} =& \int_{-\infty}^{\infty} \left[\frac{\partial I}{\partial x_j} + I \frac{\partial}{\partial \epsilon} \left(\frac{\partial \epsilon}{\partial x_j} \right) \right] \bar{G}_{\mathrm{s,R,c}}(\epsilon_t - \epsilon) \, \mathrm{d}\epsilon \\
&+ \frac{\partial \epsilon_t}{\partial x_j} \int_{-\infty}^{\infty} I \frac{\mathrm{d}\bar{G}_{\mathrm{s,R,c}}(\epsilon_t - \epsilon)}{\mathrm{d}(\epsilon_t - \epsilon)} \, \mathrm{d}\epsilon \\
&- \int_{-\infty}^{\infty} I \frac{\partial \epsilon}{\partial x_j} \frac{\mathrm{d}\bar{G}_{\mathrm{s,R,c}}(\epsilon_t - \epsilon)}{\mathrm{d}(\epsilon_t - \epsilon) \, \mathrm{d}\epsilon}
\end{aligned} \tag{35}$$

where x_j is a state vector element and $I \equiv I_{\mathrm{s,R,c}}(\mathbf{x}(\epsilon_t))$. Molecular concentrations have no effect on tangent pressure causing $\partial \epsilon / \partial x_j = 0$, simplifying (35) considerably. The HPBW in tangent pressure is dependent on the limb tangent temperature profile and the angular derivatives with respect to temperature in (35) are given by [8]

$$\begin{aligned}
\frac{\partial \epsilon}{\partial f_{lm}^T} &= \frac{\tan \epsilon}{R_t} \frac{\partial R_t}{\partial f_{lm}^T} \\
\frac{\partial}{\partial \epsilon} \left(\frac{\partial \epsilon}{\partial f_{lm}^T} \right) &= \frac{2 + \tan^2 \epsilon}{R_t} \frac{\partial R_t}{\partial f_{lm}^T} + \frac{\eta_l^T \eta_m^T}{T_t}
\end{aligned} \tag{36}$$

where T_t is temperature at the limb tangent. Contributions from $\partial \mathcal{N}_t / \partial T$ have been neglected. Expanded forms including $\partial \mathcal{N}_t / \partial T$ are in [8], but numerical experiments show that these contributions can be ignored. The antenna gain Jacobian, $\mathrm{d}\bar{G}_{\mathrm{s,R,c}}(\epsilon_t - \epsilon)/\mathrm{d}(\epsilon_t - \epsilon)$ is evaluated using the Fourier transform derivative property

$$\mathcal{F}t \left(\frac{\mathrm{d}\bar{G}_{\mathrm{s,R,c}}(\epsilon - \epsilon_t)}{\mathrm{d}\epsilon - \epsilon_t} \right) = iq \mathcal{F}t(\bar{G}_{\mathrm{s,R,c}}(\epsilon - \epsilon_t)) \tag{37}$$

where q is the aperture coordinate measured in number of wavelengths and $i = \sqrt{-1}$.

IX. COMBINE SIDEBANDS

The antenna radiances for the upper and lower sidebands are summed according to

$$I_{\mathrm{R,c}}(\mathbf{x}(\epsilon_t)) = r_{\mathrm{u,R,c}} I_{\mathrm{u,R,c}}(\mathbf{x}(\epsilon_t)) + r_{\mathrm{l,R,c}} I_{\mathrm{l,R,c}}(\mathbf{x}(\epsilon_t)). \tag{38}$$

X. SCAN MOTION RADIANCES

The EOS MLS continuous motion scan adds vertical smoothing through the time integral in (1). In the absence of jitter (unwanted deviations from uniform linear motion),

the scan motion behaves like an additional broadening of the antenna HPBW. However the $\mathcal{F}t$ algorithm described in Section VIII cannot be used because the amount of vertical smearing varies with height. Since the effect is smaller than the antenna HPBW (except for the THz scan through the troposphere whose measurements are not used in Level 2 processing), we chose to neglect it in v1.51, but is considered in subsequent versions. In the absence of jitter the error is proportional to second derivative in radiance or typically less than 0.15 K (some exceptions are noted in [8]).

Postlaunch analysis of the GHz scan encoder data [17] has revealed that there is ~8-arcsecond jitter peak-to-peak. Because of this jitter, radiance calculation errors could be as high as 0.7 K where the vertical gradient in the radiance growth is greatest. The impact of this jitter is estimated to be minor for upper tropospheric species CO and O_3, retrieved on six levels per decade change in pressure. For these molecules the estimated uncertainty from Level 2 should increase by 10%.

XI. ADD BASELINE

The final operation is adding $\mathrm{BL}_{\mathrm{R},t}$ to the result from Section X. Baseline is a spectrally flat additive quantity that empirically accounts for unmodeled instrument artifacts such as errors in evaluating the $(I_{\mathrm{bl}})_{\mathrm{R,c}}$ term. Although such errors are not expected to be scan dependent, experience from both UARS and EOS MLS experiments have shown that retrieved $\mathrm{BL}_{\mathrm{R},t}$ has vertical structure possibly suggesting an atmospheric component or a temporal/scan-dependent instrumental effect. Baseline is added to the scan motion radiance result given in (1). The instrument radiance calculation is complete.

XII. SCAN RESIDUAL MODEL

The encoder on the antenna pointing mechanism provides the limb FOV pointing angle for each 1/6-s radiance integration period. It is straightforward to derive the limb tangent height from the antenna FOV pointing angles. The successive differences between these heights when combined with the limb tangent pressure—retrievable from the radiances—are used to estimate the temperature between the scan measurements. Over altitude regions where there are no direct radiance measurement of pressure, the scan measurements are used to infer the tangent pressure using a temperature profile from other data. Optimal estimation is used to combine the information supplied by the radiances, the scan height measurements, and other auxiliary data [4]. Only the scan model algorithm is given here.

The model for fitting the Level 1 GHz and THz pointing tangent heights (Section II-B) is

$$\vec{0} = [U_r(\vec{R}_t) - \Delta U_r(\vec{\zeta}_t) - U_r(R_{\mathrm{ref}})]/\mathsf{g} \tag{39}$$

where $\vec{0}$ is the scan residual, $U_r(\vec{R}_t)$ is the geopotential [8] of $\vec{R}_t$, $\Delta U_r(\vec{\zeta}_t)$ is the geopotential difference of the tangent pressure relative to 100 hPa, $Z_{\mathrm{refgeopot}}$ is the geopotential height of 100 hPa, $U_r(R_{\mathrm{ref}})$ and R_{ref} are the geopotential and geometric height of $Z_{\mathrm{refgeopot}}$, and $\mathsf{g} = 9.806\,65\ \mathrm{ms}^{-2}$, The refracted GHz or THz pointing tangent height, $\vec{R}_t$, is

$$\vec{R}_t = \frac{\vec{R}_{\mathrm{geom}}}{\vec{\mathcal{N}}_t} \tag{40}$$

where $\vec{R}_{\text{geom}}$ is the Level 1 GHz or THz pointing tangent height. The scan residual has units of meters with an uncertainty equal to the root sum square of the covariances of all the quantities used to compute tangent height. The model for the Level 1 pointing heights is cast into a residual (a measurement defined as 0 m for each scan measurement) so as to get all the state vector-dependent quantities on the right-hand side of (39). The uncertainty of the residual is that of the Level 1 pointing tangent heights.

The geopotential difference of the tangent pressure relative to 100 hPa is the second term in the denominator of (5),

$$\Delta U(\vec{\zeta}_t) = \mathsf{k} \ln 10 \sum_l^{\text{NH}^T} \sum_m^{\text{NP}^T} \left(f_{lm}^T \eta_m^T(\vec{\phi}_t) P_l(\vec{\zeta}_t) \right). \quad (41)$$

The reference geopotential is computed from the reference geometric height, which relates to the reference geopotential height, $Z_{\text{refgeopot}}$, according to

$$R_{\text{ref}} = \frac{g^{\oplus}(\overset{\star}{R}\oplus)^2}{g^{\oplus}\overset{\star}{R}\oplus - \mathsf{g}Z_{\text{refgeopot}}} - \overset{\star}{R}\oplus + R^{\oplus} \quad (42)$$

where $g^{\oplus}$ is the gravitational acceleration at the Earth's surface, $R^{\oplus}$ is the Earth radius, $Z_{\text{refgeopot}} = \sum_m^{\text{NH}^T} f_m^{\text{refgeopot}} \eta_m^T(\vec{\phi}_t)$, and $f_m^{\text{refgeopot}}$ are the reference geopotential heights on the temperature measurement track angles.

Formulas for the Jacobians of the scan residual with respect to the limb tangent pressure, temperature and reference geopotential are

$$\frac{\partial \vec{0}}{\partial \vec{\zeta}_t} = \mathsf{k} \ln 10 \sum_l^{\text{NH}^T} \sum_m^{\text{NP}^T} f_{lm}^T \eta_m^T(\vec{\phi}_t) \eta_l^T(\vec{\zeta}_t)/[\mathsf{g}\mathcal{M}(\vec{\zeta}_t)]$$
$$+ \frac{dU_r}{d\vec{R}_t} \frac{\vec{R}_t}{\mathsf{g}\vec{\mathcal{N}}_t} \left[(\vec{\mathcal{N}}_t - 1)\left(\ln 10 + \frac{d\ln \vec{T}_t}{d\vec{\zeta}_t}\right) \right.$$
$$+ \left. \frac{0.3733 \vec{f}_t^{H_2O}}{\vec{T}_t 10^{\vec{\zeta}_t}} \left(\frac{d\ln \vec{f}_t^{H_2O}}{d\vec{\zeta}_t} - \frac{d\ln \vec{T}_t}{d\vec{\zeta}_t} \right) \right]$$

(43)

$$\frac{\partial \vec{0}}{\partial f_{lm}^T} = \frac{\mathsf{k}\ln 10}{\mathsf{g}} \eta_m^T(\vec{\phi}_t)\eta_l^T(\vec{\zeta}_t)$$
$$+ \frac{dU_r}{d\vec{R}_t} \frac{\vec{R}_t\left(\vec{\mathcal{N}}_t - 1 + \frac{0.3733\vec{f}_t^{H_2O}}{\vec{T}_t^2 10^{\vec{\zeta}_t}}\right)}{\mathsf{g}\vec{T}_t\vec{\mathcal{N}}_t}$$
$$\times \eta_l^T(\vec{\zeta}_t)\eta_m^T(\vec{\phi}_t) \quad (44)$$

$$\frac{\partial \vec{0}}{\partial f_m^{\text{refgeopot}}} = \frac{dU_r}{dR_{\text{ref}}} \eta_m^T(\vec{\phi}_t)$$
$$\times \frac{R_{\text{ref}} - R^{\oplus} + \overset{\star}{R}\oplus}{g^{\oplus}\overset{\star}{R}\oplus - \mathsf{g}\sum_m^{\text{NH}^T} f_m^{\text{refgeopot}}\eta_m^T(\vec{\phi}_t)}. \quad (45)$$

The tangent pressure Jacobian is a sum of two contributions. The first term is a hydrostatic contribution and the second two terms are an index of refraction contribution. When $R_t < R^{\oplus}$, the second two terms are zero. Water vapor Jacobians are ignored in the scan residual model.

TABLE II
SUMMARY OF FORWARD MODEL APPROXIMATIONS

Approximation	Section	Purpose	Impact
Representation basis functions.	III	A[1]	T[2]
PSIG driven quadrature.	IV	A	T
Hydrostatic balance.	IV	N[3]	…[4]
Co-alignment of orbital and LOSF planes.	IV	N	…
Equivalent circular Earth.	[8]	A	< 0.01K
Neglect refraction in LOS ϕ_t	IV	O[5]	…
Neglect refraction on path ϕ	IV	A	…
Minimum ζ_t and h_t are coincident.	[8]	N	…
Summed line × line Van Vleck Huber Voigt lineshape.	V	D[6]	…
Estimated values for some spectroscopic parameters.	[8]	N	…
Line selection thresholds	V	A	T
Refractive path length scaling	VI	A	< 0.01K
LOS rays reflect off the reference geopotential surface ignoring surface topography.	VI	D	…
Separate frequency and spatial integrations	VII	A	NEG[7]
Neglect 2nd IF image sideband in DACS spectral integration	[8]	A	…
Neglect radiance cross track gradients in FOV.	VIII	N	…
Antenna pattern elevation axis is in the LOSF plane	[8]	A	NEG
Antenna pattern is scan independent	[8]	A	< 0.5K
FFT approximation to antenna radiance	VIII	A	NEG
Empirical geocentric satellite height for the equivalent circular Earth.	[8]	A	NEG
Neglect difference between scanned ϕ_t and instantaneously observed FOV ϕ_t	[8]	A	…
L2PC linear radiance model	XIII	A	…

[1] A is an approximation that helps simplify a calculation or improves an interface to the retrieval program.

[2] T is a tunable approximation.

[3] N is a necessary approximation due to incomplete knowledge.

[4] ··· is an unknown error that is zero under certain conditions. For example, neglecting refraction in the calculation of ϕ or ϕ_t only has error for a horizontally inhomogeneous atmosphere.

[5] O is an approximation caused by an oversight during the software development that will be corrected in future versions.

[6] D is discretionary choice. For example, detailed models describing reflectivities over various surface types with consideration of varying topographies have not been investigated at this time. Hence, a simple surface reflectivity model is used as a placeholder for more sophisticated models to be added in future versions.

[7] NEG is an unquantified uncertainty that can be shown to have much less impact than the uncertainty associated with its instrumental parameter. For example, the error introduced by separating the frequency and spatial integrations neglects, in the worst case, a 0.4% HPBW change across a 500-MHz-wide filter at 118 GHz, which is small compared to the few percent uncertainty in the measured HPBW [17], [18]

XIII. LEVEL 2 PROCESSING COEFFICIENTS FILE

The EOS MLS forward model does not run quickly enough to permit its usage for all the EOS MLS channels used in Level 2 processing. Many of the EOS MLS channels target weak emitters (e.g., BrO and ClO) whose radiances scale linearly with concentration. For these situations, the forward model can be replaced with a first order Taylor series where the radiances and Jacobians are calculated off-line with the EOS MLS forward model. The Level 2 Processing Coefficients (L2PC) file contains the first order Taylor series coefficients of (1) given by

$$\overset{\bullet}{I} - I_{bl} = \overset{\star}{I} + \sum_j \frac{\partial \overset{\star}{I}}{\partial x_j}(x_j - \overset{\star}{x}_j) \qquad (46)$$

where x_j is a state vector element, $\overset{\star}{x}_j$ is a linearization state vector element and $\overset{\star}{I}$ is the calculated radiance (Sections II–IX) at the linearization state vector. The state vector contains species and temperature profiles. In future versions of the forward model, spectroscopic parameters (position and line-shape), will be added to the state vector. Currently, the L2PC calculation includes radiances and Jacobians for profiles from five adjacent LOS angles with the tangent LOS tangent angle coaligned with the center basis ϕ. Radiances are computed for 76 tangent pressures between 10^3 and 10^{-5} hPa. Estimated model radiances are evaluated using (46) at all the tangent pressures in the L2PC state vector. The resulting radiances are interpolated to the measured tangent pressures with cubic splines. Jacobians for the retrieval are interpolated to the measured tangent pressures with linear interpolation.

XIV. INTERPRETING BASIS COEFFICIENTS

A feature of the EOS MLS forward model is that it runs at the "resolution" of the retrieved representations. The piecewise-linear functionality of the representations is fully embedded throughout the entire forward model calculation. The benefits of this approach are it minimizes the number of Jacobians to compute and there are no transformation errors introduced by converting coarsely gridded representation functions into finely gridded layer means. It should be appreciated that the piecewise-linear representation is an approximation to the true atmosphere. The averaging kernel widely used in retrieval theory [32] will not capture the full extent of the smoothing because it is calculated at the resolution of the retrieval representation with this forward model. Therefore, an additional smoothing component from the forward model is required. Consider a linearized forward model represented by

$$I = \overset{\star}{I} + (f - \overset{\star}{f} \eta)H \qquad (47)$$

where $\mathbf{H} = \partial \overset{\star}{I} / \partial f$ is the radiance Jacobian in the limit of infinite resolution, the same as the true atmosphere f, η is a matrix containing the representation basis function values described in Section III, and $\overset{\star}{f}$ is the linearization representation at the retrieval resolution. The retrieval Jacobian used for computing the averaging kernel is $\overset{\star}{\mathbf{K}} = \mathbf{H}\eta$. It is required that the forward model responds linearly to fine structure fluctuations of f that are not captured by the representation basis resolution.

If the forward model has no errors apart from those introduced by the limited resolution of the representations, the atmospheric radiances are related to the modeled radiances according to

$$I - \overset{\star}{I} = (f - \overset{\star}{f} \eta)H \approx (\hat{f} - \overset{\star}{f})\eta H \qquad (48)$$

where $\hat{f}$ is the forward model's approximation of the true atmosphere. The right-hand side having fewer degrees of freedom can only be an approximate solution. The $\overset{\star}{f} \eta H$ is common to both sides and can be dropped out leaving

$$fH \approx \hat{f}\eta H \qquad (49)$$

Over that portion of representation coefficients of $\hat{f}$ where $(\mathbf{HH}^t)^{-1}$ is invertible it is easy to show that

$$\hat{f} = f\eta^t(\eta\eta^t)^{-1} \qquad (50)$$

minimizes the sum of squared differences between the model and true radiances. The forward model smoothing effect is a least squares fit of the coarsely gridded representation to the true representation given by $\eta^t(\eta\eta^t)^{-1}$. The full averaging kernel is the product of the retrieval averaging kernel which accounts for the degradation of resolution caused by random errors associated with the measurements and forward model, and the least squares matrix which describes the smoothing effect caused by finite sampling.

XV. FORWARD MODEL COMPARISONS AND EXAMPLES OF MEASURED AND FITTED SPECTRA

Ensuring the accurate implementation of the EOS MLS forward model algorithm into computer code is done through intercomparison. At JPL, we independently coded the EOS MLS forward model algorithm in FORTRAN-90 and Interactive Data Language (IDL) computer languages. The IDL forward model includes a few more approximations than the FORTRAN-90 forward model. The MLS team at the University of Edinburgh also has its own forward model which is used for comparisons and quality checking. The Edinburgh model is a 1-D radiative transfer model having an independent spectroscopy interface with its own line selection method. The Edinburgh model uses the same instrument response functions. Detailed comparisons are performed periodically. The FORTRAN-90 and IDL codes compare very favorably, within a few tenths of 1 K in the stratosphere increasing to 3–4 K in the upper troposphere. These differences are consistent with the unrefracted path segment approximation (neglecting 20) in the IDL model. Comparisons of a 1-D run of the EOS MLS forward model with the Edinburgh model show good agreement (a few tenths) in the stratosphere and mesosphere. Agreement degrades to a few Kelvin in the troposphere. The cause of this is likely due to differences in the line selection and continuum spectroscopy used. The Jacobian calculation is checked by intercomparing results between the IDL and FORTRAN-90 models and comparing both to Jacobians calculated using finite differences. The finite difference computation of Jacobians is accomplished by perturbing each state vector element one at a time and dividing the change in radiance by the perturbation—a capability of the Level 2 software [4]. In all instances, the agreement is excellent ensuring that the algorithm and coding have been successful.

Fig. 4 shows six examples of signals measured by EOS MLS. Each spectrum is an average of one day's (3495) spectra from a selected 1/6-s measurement whose FOV direction points approximately at the tangent height indicated. The retrieval uses a subset of good measured radiances. The reasons for this are: 1) to avoid correlated noise in the measurements, the Level 2 processing only uses nonspectrally overlapping channels; 2) due to computer processing limitations, some nonlinear channels that are time consuming to evaluate are omitted; 3) some channels that are modeled with L2PC files are omitted when their radiances become nonlinear; and 4) some channels where there is evidence that the EOS MLS is affected by RF interference.

The radiance residuals show that the measurements are being fit to about 1% of the signal except for band 19 which is closer to 10%, but they also show spectral features larger than the noise. The cause of the differences could be due to many factors such as spectroscopic errors, instrument calibration/characterization errors, or retrieval performance errors. Further discussion of these issues is beyond the scope of this paper but understanding them is actively being investigated by the MLS team. It is worth noting that Bands 6 and 27 in R2 and Band 12 in R4 use the L2PC linear model described in Section XIII. Bands 13, 14, 30, and 31 in R4 target HCl, O_3, HO_2, and BrO. The lines of HO_2 and BrO are too small to see on the scale of this figure, but are shown in [2, Fig. 15].

XVI. SUMMARY AND FUTURE WORK

The EOS MLS instrument radiance and scan model algorithms including the analytic calculation of Jacobians have been presented. Table II summarizes the approximations made by the instrument radiance model.

Forward model improvements are underway. Approximations associated with refraction on the horizontal evaluation of profiles are being replaced with more exact calculations. A better handling of the continuous scan is under development. Updates for molecular line data are being made to the JPL catalog and new line width parameters measurements are being added to the EOS MLS catalog. The EOS MLS catalog will be regenerated with weaker line selection thresholds. This will improve the modeling of weaker signals. The additional lines will slow the forward model calculation significantly. This issue is being addressed by adding a Pre-Frequency Averaging (PFA) approximation. PFA uses channel-averaged cross-section tables and simplifies or eliminates the filter quadrature calculation. PFA was successfully used for all the weak signal bands in UARS MLS [8]. The PFA implementation for EOS MLS has a mixed mode capability which permits the rapid calculation of weak signals in the presence of strong ones accurately (e.g., HNO_3 on the strong wing of O_3).

REFERENCES

[1] J. W. Waters, W. G. Read, L. Froidevaux, R. Jarnot, R. E. Cofield, D. A. Flower, G. K. Lau, H. M. Pickett, M. L. Santee, D. L. Wu, M. A. Boyles, J. R. Burke, R. R. Lay, M. S. Loo, N. J. Livesey, T. A. Lungu, G. L. Manney, L. L. Nakamura, V. S. Perun, B. P. Ridenoure, Z. Shippony, P. H. Siegel, R. P. Thurstans, R. S. Harwood, H. C. Pumphrey, and M. J. Filipiak, "The UARS and EOS Microwave Limb Sounder experiments," *J. Atmos. Sci.*, vol. 56, pp. 194–218, 1999.

[2] J. W. Waters, L. Froidevaux, R. S. Harwood, R. F. Jarnot, H. M. Pickett, W. G. Read, P. H. Siegel, R. E. Cofield, M. J. Filipiak, D. A. Flower, J. R. Holden, G. K. Lau, N. J. Livesey, G. L. Manney, H. C. Pumphrey, M. L. Santee, D. L. Wu, D. T. Cuddy, R. R. Lay, M. S. Lou, V. S. Perun, M. J. Schwartz, P. C. Stek, R. P. Thurstans, M. A. Boyles, K. M. Chandra, M. C. Chavez, G.-S. Chen, B. V. Chudasama, R. Dodge, R. A. Fuller, M. A. Girard, J. H. Jiang, Y. Jiang, B. W. Knosp, R. C. LaBelle, J. C. Lam, K. A. Lee, D. Miller, J. E. Oswald, N. C. Patel, D. M. Pukala, O. Quintero, D. M. Scaff, W. V. Snyder, M. C. Tope, P. A. Wagner, and M. J. Walch, "The Earth Observing System Microwave Limb Sounder (EOS MLS) on the Aura satellite," *IEEE Trans. Geosci. Remote Sens.*, vol. 44, no. 5, pp. 1075–1092, May 2006.

[3] R. F. Jarnot, V. S. Perun, and M. J. Schwartz, "Radiometric and spectral performance and calibration of the GHz bands of EOS MLS," *IEEE Trans. Geosci. Remote Sens.*, vol. 44, no. 5, pp. 1131–1143, May 2006.

[4] N. J. Livesey, W. V. Snyder, W. G. Read, and P. A. Wagner, "Retrieval algorithms for the EOS Microwave Limb Sounder (MLS)," *IEEE Trans. Geosci. Remote Sens.*, vol. 44, no. 5, pp. 1144–1155, May 2006.

[5] N. J. Livesey and W. G. Read, "Direct retrieval of line-of-sight atmospheric structure from limb sounding observations," *Geophys. Res. Lett.*, vol. 27, pp. 891–894, 2000.

[6] D. L. Wu, J. H. Jiang, and C. P. Davis, "EOS MLS cloud ice measurements and cloudy-sky radiative transfer model," *IEEE Trans. Geosci. Remote Sens.*, vol. 44, no. 5, pp. 1156–1165, May 2006.

[7] M. J. Schwartz, W. G. Read, and W. V. Snyder, "EOS MLS forward model polarized radiative transfer for Zeeman-split oxygen lines," *IEEE Trans. Geosci. Remote Sens.*, vol. 44, no. 5, pp. 1182–1191, May 2006.

[8] W. G. Read, Z. Shippony, and W. V. Snyder, "EOS MLS forward model algorithm theoretical basis document," Jet Propulsion Lab., Pasadena, CA, 2003. [Online]. Available: http://swdev.jpl.nasa.gov/doc.htm#ATBDs.

[9] N. J. Livesey, W. G. Read, L. Froidevaux, J. W. Waters, H. C. Pumphrey, D. L. Wu, M. L. Santee, Z. Shippony, and R. F. Jarnot, "The UARS Microwave Limb Sounder version 5 dataset: Theory, characterization and validation," *J. Geophys Res.*, vol. 108, no. D13, p. 4378, 2003. DOI: 10.1029/2002JD002273.

[10] W. G. Read, J. W. Waters, D. L. Wu, E. M. Stone, Z. Shippony, A. C. Smedley, C. C. Smallcomb, S. Oltmans, D. Klev, H. G. J. Smit, J. Mergenthaler, and M. K. Karki, "UARS MLS upper tropospheric humidity measurement: Method and validation," *J. Geophys. Res.*, pp. 32 207–32 258, 2001.

[11] F. T. Barath, M. C. Chavez, R. E. Cofield, D. A. Flower, M. A. Frerking, M. B. Gram, W. M. Harris, J. R. Holden, R. F. Jarnot, W. G. Kloezeman, G. J. Klose, G. K. Lau, M. S. Loo, B. J. Maddison, R. J. Mattauch, R. P. McKinney, G. E. Peckham, H. M. Pickett, G. Siebes, F. S. Soltis, R. A. Suttie, J. A. Tarsala, J. W. Waters, and W. J. Wilson, "The Upper Atmosphere Research Satellite Microwave Limb Sounder: Instrument," *J. Geophys. Res.*, vol. 98, pp. 10 751–10 762, 1993.

[12] S. A. Buehler, P. Eriksson, T. Kuhn, A. von Engelin, and C. Verdes, "ARTS, the atmospheric radiative transfer simulator," *J. Quant. Spectrosc. Radiat. Transf.*, vol. 91, pp. 65–93, 2005.

[13] P. Eriksson and S. Bühler. (2005) ARTS User Guide. [Online]. Available: http://www.sat.uni-bremen.de/arts/arts2/doc/uguide/uguide.pdf

[14] The Karlsruhe Optimized and Precise Radiative Transfer Algorithm (KOPRA) [Online]. Available: http://www-imk.fzk.de/asf/ame/publications/kopra-docu/

[15] T. Steck, M. Hopfner, T. von Clarmann, and U. Grabowski, "Tomographic retrieval of atmospheric parameters from infrared limb emission observations," *Appl. Opt.*, vol. 44, no. 16, pp. 3291–3301, 2005.

[16] W. J. Reburn, V. L. Jay, R. Siddans, and B. J. Kerridge, "Retrievals of O3 and H2O in the lower stratosphere and troposphere from EN-VISAT," Eur. Space Agency, Noordwijk, The Netherlands, Tech. Rep. ESA SP-572, 2004.

[17] R. E. Cofield and P. C. Stek, "Design and field-of-view calibration of 114–660-GHz optics of the Earth Observing System Microwave Limb Sounder," *IEEE Trans. Geosci. Remote Sens.*, vol. 44, no. 5, pp. 1166–1181, May 2006.

[18] H. M. Pickett, "Microwave Limb Sounder THz module on Aura," *IEEE Trans. Geosci. Remote Sens.*, vol. 44, no. 5, pp. 1122–1130, May 2006.

[19] C. C. Tscherning, Ed., *The Geodesist's Handbook*: Bureau Central De L'Assoc. Int. De Géodsié, 1984, vol. 58.

[20] R. J. List, *Smithsonian Meteorological Tables*. Washington, DC: Smithsonian Inst., 1951, p. 114. Smithson. Misc. Collect..

[21] H. M. Pickett, R. L. Poynter, E. A. Cohen, M. L. Delitsky, J. C. Pearson, and H. S. P. Muller, "Submillimeter, millimeter, and microwave spectral line catalog," *J. Quant. Spectrosc. Radiat. Transf.*, vol. 60, no. 5, pp. 883–890, 1998.

[22] L. S. Rothman, C. P. Rinsland, A. Goldman, S. T. Massie, D. P. Edwards, J. M. Flaud, A. Perrin, C. Camy-Peyret, V. Dana, J. Y. Mandin, J. Schroeder, A. McCann, R. R. Gamache, R. B. Wattson, K. Yoshino, K. V. Chance, K. W. Jucks, L. R. Brown, V. Nemtchinov, and P. Varinasi, "The HITRAN molecular spectroscopic database and HAWKS (HITRAN atmospheric workstation): 1996 edition," *J. Quant. Spectrosc. Radiat. Transf.*, vol. 60, p. 665, 1998.

[23] P. Kroopnick and H. Craig, "Atmospheric oxygen: Isotopic composition and solubility fractionation," *Science*, vol. 175, pp. 54–55, 1972.

[24] A. Meshkev and F. DeLucia, private communication, 2004.

[25] H. M. Pickett, private communication, 2004.

[26] J. R. Pardo, E. Serabyn, and J. Cernicharo, "Submillimeter atmospheric transmission measurements on mauna kea during extremely dry El Niño conditions: Implications for broad-band opacity contributions," *J. Quant. Spectrosc. Radiat. Transf.*, vol. 68, pp. 419–433, 2001.

[27] D. L. Huber and J. H. V. Vleck, "The role of Boltzmann factors in line shape," *Rev. Mod. Phys.*, vol. 38, no. 1, pp. 187–204, 1966.

[28] M. A. Janssen, *An Introduction to the Passive Microwave Remote Sensing of Atmospheres*. New York: Wiley, 1993, ch. 1, pp. 1–35.

[29] M. J. Schwartz, W. V. Snyder, and W. G. Read, "Mesosphere-specific forward model algorithm theoretical basis document," Jet Propulsion Lab., Pasadena, CA, Overview ATBD, JPL D-28534, version 1.0, Jun. 15, 2004.

[30] J. D. Kraus, *Radio Astronomy*. New York: McGraw-Hill, 1966.

[31] M. Born and E. Wolf, *Principles of Optics*. New York: MacMillan, 1964.

[32] C. D. Rodgers, "Characterization and error analysis of profiles retrieved from remote sounding measurements," *J. Geophys. Res.*, vol. 95, no. D5, pp. 5587–5595, 1990.

William G. Read was born in Rockville Centre, NY, on April 14, 1957. He received the A.B. degree from Occidental College, Los Angeles, CA, and the Ph.D. degree in physical chemistry from the University of Illinois, Urbana, in 1979 and 1983, respectively.

From 1983 to 1985, he held an NRC-NASA Resident Research Associateship award at the Jet Propulsion Laboratory, Pasadena, CA, and then became a JPL employee. Currently, he is a Principal Research Scientist and a Co-Investigator for the NASA Earth Observing System Microwave Limb Sounder.

Zvi Shippony, photograph and biography not available at the time of publication.

Michael J. Schwartz began his undergraduate education at Deep Springs College, Deep Springs, CA. He received the B.A. degree in physics from Carleton College, Northfield, MN, and the Ph.D. degree in physics from the Massachusetts Institute of Technology (MIT), Cambridge, in 1985 and 1998, respectively. His thesis, supervised by Prof. D. H. Staelin, involved atmospheric remote sensing with millimeter-wave oxygen lines.

He was on the research staff of the MIT Research Laboratory of Electronics in 1999, where he contributed to the development of an aircraft-based atmospheric sounding package. In 2000, he joined the Microwave Limb Sounding Group at the Jet Propulsion Laboratory. His responsibilities included the development of digital autocorrelator spectrometer hardware and processing algorithms for the EOS-MLS instrument, oversight of the MLS temperature and geopotential height data products, and development of the polarized forward model for Zeeman-split oxygen lines.

Nathaniel J. Livesey was born in 1970 in Cambridge, U.K. He received the B.A. (Hons.) degree in physics, and the Dr.Phil. degree in atmospheric physics from the University of Oxford, Oxford, U.K., in 1991 and 1995, respectively.

Since 1996, he has been a Member of the Microwave Atmospheric Science Team at the Jet Propulsion Laboratory, California Institute of Technology, Pasadena, and is a Co-investigator for the Earth Observing System Microwave Limb Sounder.

W. Van Snyder received degrees in computer science and applied mathematics.

He has been at the Jet Propulsion Laboratory, Pasadena, CA, since July 1967. Until 1996, he has worked on development of libraries of mathematical software. Since then he has worked on ground software to analyze the data from satellite remote sensing instruments, including Topex/Poseidon, NSCAT/QuikScat, and Aura/MLS. He has served as an Adjunct Associate Professor of computer science at West Coast University from 1976 to 1992 and as a delegate to and officer of the ANSI and ISO Fortran committees since 1997. He has been an Associate Editor for the *ACM Transactions on Mathematical Software* since 1994